Structure, Mechanics and Failure of Stochastic Fibrous Networks: Part I—Microscale Considerations

C. W. Wang

L. Berhan

A. M. Sastry

Department of Mechanical Engineering and
Applied Mechanics,
The University of Michigan,
Ann Arbor, MI 48109-2125

Applications for porous fibrous materials range from electrochemical substrates to web reinforcement in polymeric composite materials. The details of local load transfer are studied in a class of cost-effective, stochastic fibrous networks used in battery applications, which form the substrate for a composite electrode. The connectivity of these materials is quantitatively related to modulus and strength, and detailed results of different simulations approaches in approximating material construction are discussed. In Part I, we discuss microscale assumptions, including beam type, nodal connections and equivalence of models to more physically realistic models. Simulation of large networks is computationally intensive, and show low-strain, nonlinear behavior even when comprised of elastic elements when failure criteria (here, strength-of-materials) are applied to produce sequential rupture of beams and nodes. Strategies for effective simulation of these materials requires detailed analysis of the simplest assumptions which can be made at the microscale which produce acceptably realistic response. We show that simple Euler-Bernoulli beam elements can be used to effectively model such materials, even when segment lengths in a network are very small. Moreover, connections comprised of simple torsion springs produce realistic behavior, and can mimic more realistic junctures by adaptation of the linear solution to a compliant zone model. In Part II of this work, we demonstrate the effect of model selection on full network behavior, and also discuss issues of connectivity at the scale of the porous material rather than element-by-element. This work points toward use of simple constructions to model complex behavior, and may ultimately provide insight into modeling of a large class of porous materials.
[S0094-4289(00)01704-7]

1 Introduction

Porous nonwoven fibrous materials comprise a promising class of materials for use as electrochemical substrates in at least two battery technologies: Ni/MH (nickel-metal hydride) and Li-ion (lithium ion) cells. High energy densities demand low-density battery materials, and thus porous substrates with low volume fraction of conductive mass (as low as 3 percent for positive plate substrates in Ni/MH cells, for example, such as that shown in Fig. 1) are desirable. For such highly porous structures, it is critical to determine whether a given morphology and density of particles creates a "percolated" network, i.e., a network in which there are continuous, domain-spanning (edge-to-edge) paths of material. If there are no, or few, such paths, conductivity is negligible as measured across the electrode. The details of load transfer in the materials are thus also of central interest, since local failure phenomena initiated by mechanical loads induced by electrochemical cycling can reduce connectivity in these conductive webs, and thus critically reduce transport properties. If conductivity in substrate materials for battery electrodes is not sufficiently high, the battery will fail to discharge to an acceptable capacity, or fail entirely [1]. Thus, the present interest (including [2]) is in understanding micromechanical failure mechanisms, in order to design superior electrochemical materials, and also satisfactorily predict lifetime and degradation.

Previous work on the mechanics of similar point-bonded fibrous networks can be roughly divided into four main areas [3]. 1)

continuum approximations of behavior using unit cell approaches [4,5], including work on development of other applications for solutions of Laplace's equation, e.g., conductivity of porous media or gasses (with much of the classic work summarized in the excellent review by Meredith and Tobias [6]); 2) micromechanical models employing averaging assumptions to examine fibrous networks [7–11] (with affine deformations of unit cells of known orientation relative to the direction of applied load); 3) numerical models employing various network generation techniques, to ultimately gain a continuum description of behavior [12–16]; and 4) purely statistical approaches, involving tracking progressive local failures in regular periodic arrays with statistically-assigned element properties [17].

The present general approach for generation of model microstructures has been described in detail previously [1,3,4,18–20]. Work-to-date has been guided by mechanical and transport properties along with detailed image analysis of battery materials. The distinguishing features of the work compared with other efforts in nonwovens is that microstructures have been characterized quantitatively and statistically. Also, specific, morphology-driven failure mechanisms observed in battery substrates have been incorporated directly into numerical models [19,21], with success in predicting both trends in behavior and quantitative properties. These studies [19,20] have shown that the details of load transfer are key in predicting material properties. In NiMH cells, for example, the strength and stiffness of fiber-fiber bonds can change significantly due to electrodeposition during electrochemical reactions. These effects must be modeled in order to design superior materials.

Here, we focus on these details of load transfer and the damage tolerance of networks, expanding on development of an earlier
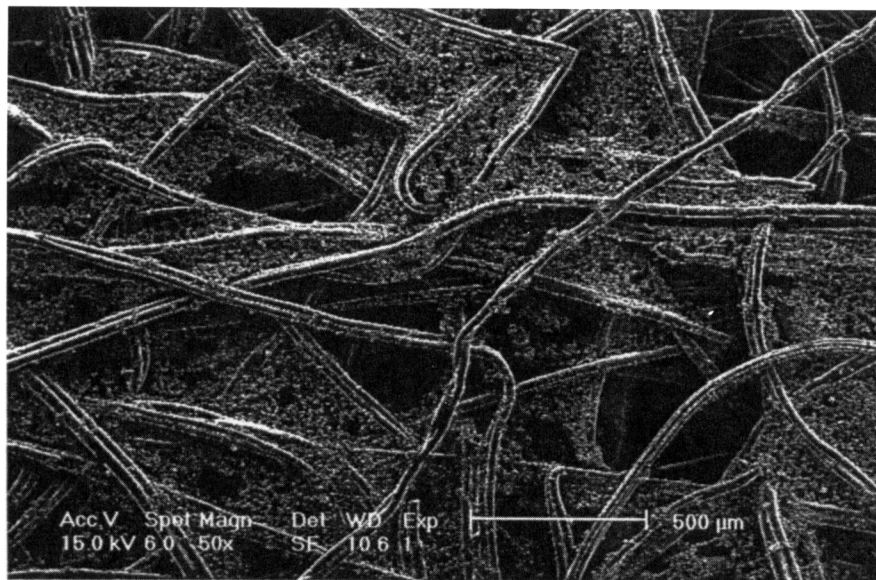
Copyright © 2000 by ASME

Fig. 1 SEM image (50×) of an NiMH positive plate substrate, produced by National Standard (Fibrex), containing 50/50 fiber/powder by weight ratio, 97 percent pure nickel by mass; calculated porosity: 82 percent; fiber diameter: 30 mm; staple lengths: 0.64–1.27 cm; content

general technique [1,3]. We also examine the effects of scale in these calculations, and present several methods for modeling connectivity in networks. Finally, we compare these calculations with results for real materials. The purpose of the present work is thus fourfold:

1 to assess the effect of choice of beam types in models for fibers, and the effect of assumptions at fiber-fiber bonds, on the simulated overall network response;

2 to examine the effect of assumptions regarding material connectivity on the simulated overall network response;

3 to examine the effects of scale in simulation, especially regarding strength and damage tolerance; and

4 to assess the ability of spring-jointed models in predicting real materials response, as compared to a class of fiber-particle networks.

Ultimately, the aim of this work is to allow design of stochastic microstructures, wherein both overall properties, and variance in properties, can be predicted. In the present paper, Part I—Microscale Considerations, we address the first two points, namely development of appropriate elemental models for the components of the network (beams and joints, respectively). In the second part of this work, Part II—Simulations and Applications, we describe results of simulations of large networks thusly constructed, and quantify the effects of these micromechanical assumptions on the response of larger networks.

2 Microscale Models

Briefly, the general technique for generating a network is as follows. A volume of fibers is chosen, and a number of fibers corresponding to the chosen volume fraction (for a given domain size) is calculated. These fibers are placed in the representative domain according to known distributions of fiber orientations, diameters, and lengths. Periodic boundary conditions are then enforced, and non-load bearing fiber "ends" are removed (Fig. 2 shows this process schematically for a single fiber in a unit cell).

Micromechanical assumptions for the elements and nodes in such networks are required in order to predict mechanical properties. Several techniques have been developed as part of this work, and are described in the following sections. In Part II of this work, we discuss the effect of each assumption on simulations for pre-

diction of properties of real substrate materials for NiMH cells, and point out certain assumptions which are robust, and requirements for elimination of scale effects in simulation of real material response.

2.1 Substrate Microstructures: Observations. Real fibrous networks such as those studied by the authors generally contain fibers which deviate from the regular arrays described: they are imperfectly bonded, nonstraight, and often mixed with other particles. In battery materials, several phases of various shape and size often comprise an electrode, with each phase having different functionality (electrochemical reactant, substrate for provision of active surface area, conductive element, mechanical strengthener or stiffener, etc.). Here, we examine the mechanics of the fibrous network only, since for many practical battery materials, the particle content is below the percolation point for spheres, so that the only percolated phase is the fibrous phase. Percolation is achieved at only 4–5 percent volume fraction for networks comprised of fibers with aspect ratios of ~100 (per Cheng and Sastry [18], validating earlier work by Kirkpatrick [22]). More-
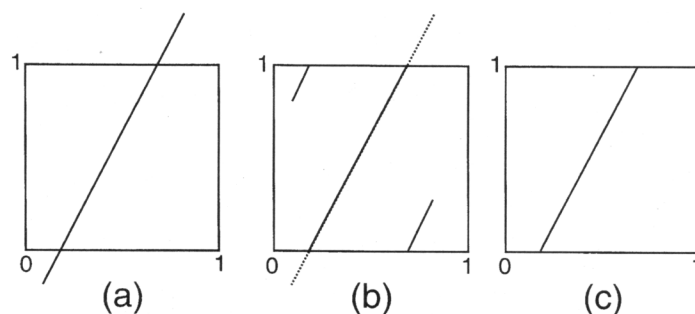

Fig. 2 Network generation approach, with a single fiber shown for simplicity. Fiber is placed in the unit cell (*a*) whereupon periodic boundary conditions are applied, effectively "wrapping" overlapping ends back into unit cell (*b*), and nondomain-spanning segments are removed, as they do not bear network loads (*c*). Notation for a two-element case, with fixed end. Location and numbering of nodes used in calculating maximum stress are shown below the two-beam schematic.

over, it is the fiber phase which is commonly used to provide both conductivity and mechanical stiffness and strength.

In a network, segments of various length are formed. If we assume that these segments, upon material processing, behave independently of one another; i.e., the staple fiber is replaced by the segment as the elemental unit, these differences in length necessitate study of internal assumptions of load in the beams.

2.2 Beam Assumptions. The beam theory is generally applicable for beams of aspect ratio greater than around 5–10. However, in generation of even moderately low volume networks, a large portion of small segments arise (see particularly Part II of this work). As the beam aspect ratio is reduced, consideration of deformation due to transverse shear is required (Timoshenko beam theory) since the simple Euler-Bernoulli beam theory overestimates stiffness for a single beam.

In fibrous networks, however, the stiffness of an array of beams is limited by the relative compliance afforded by even rigid bonds between beams. Several examples in the following sections illustrate the small differences in such arrays for Timoshenko versus Euler beams, with notation for the two-beam problem shown in Fig. 3. Generally, we derive the forces and displacements in a network as follows, with axial force F_i, transverse force S_i, and bending moment Q_i. A is the cross-section area, and I is moment of inertia. Two cases are outlined, for the Euler-Bernoulli and Timoshenko-type beam assemblies with rigid bonds. The potential energy, π, for an Euler-Bernoulli beam assembly can be written [23,24] as

$$\pi = \frac{1}{2} \int_0^L \left[EA \left(\frac{du}{dx} \right)^2 + EI \left(\frac{d^2 v}{dx^2} \right)^2 \right] dx - F_1 u(0) - F_2 u(L)$$

$$- S_1 v(0) - S_2 v(L) - Q_1 \frac{dv(0)}{dx} - Q_2 \frac{dv(L)}{dx} \tag{1}$$

The variational method yields the governing equations

$$EA \frac{d^2 u}{dx^2} = 0$$

$$EI \frac{d^4 v}{dx^4} = 0 \tag{2}$$

For rigid connections between beams, we have the boundary conditions

$$\text{at } x=0 \rightarrow \begin{cases} EA \left(\frac{du}{dx} \right) = -F_1 & \text{or } u = \text{constant} \\ EI \left(\frac{d^2 v}{dx^2} \right) = -Q_1 & \text{or } \frac{dv}{dx} = \text{constant} \\ EI \left(\frac{d^3 v}{dx^3} \right) = -S_1 & \text{or } v = \text{constant} \end{cases} \tag{3}$$

$$\text{at } x=L \rightarrow \begin{cases} EA \frac{du}{dx} = F_2 & \text{or } u = \text{constant} \\ EI \left(\frac{d^2 v}{dx^2} \right) = Q_2 & \text{or } \frac{dv}{dx} = \text{constant} \\ EI \left(\frac{d^3 v}{dx^3} \right) = S_1 & \text{or } v = \text{constant} \end{cases}$$

For Timoshenko beams joined by rigid connections, we rewrite the potential energy of the assembly as

$$\pi = \int_0^L \left\{ \left[EA \left(\frac{du}{dx} \right)^2 \right] + \left[EI \left(\frac{d\Psi}{dx} \right)^2 \right] + GAK_s \left(\Psi + \frac{dv}{dx} \right)^2 \right\} \tag{4}$$

$$- F_1 u(0) - F_2 u(L) - S_1 v(0) - S_2 v(L) - Q_1 (\Psi)_{x=0}$$

$$- Q_2 (\Psi)_{x=L}$$

where K_s is the shear correction factor, and Ψ the rotation function about the y-axis. The shear correction coefficient accounts for the difference in the assumed constant versus the actual state of shear stress in this theory and the parabolic variation of the actual, through the thickness. It can be computed as [24]

$$K_s = \frac{V^2}{A \int \tau_a^2 dA} = \frac{A_s}{A} \tag{5}$$

where V is the shear force, τ_a is the actual shear stress in the cross section, and A_s is the corresponding shear area. For the circular cross-sections of interest, we use a shear correction factor of approximately

$$K_s = \frac{3(1+v)d^2}{8L^2} \tag{6}$$

which agrees closely with the implementation in ABAQUS used in Part II of this work to solve for internal loads and displacements in networks similarly constructed. Using the variational method as before, the governing equations are obtained as

$$EA \frac{d^2 u}{dx^2} = 0$$

$$EI \frac{d^2 \Psi}{dx^2} - GAKs \left(\Psi + \frac{dv}{dx} \right) = 0 \tag{7}$$

$$GAKs \frac{d}{dx} \left(\Psi + \frac{dv}{dx} \right) = 0$$

Boundary conditions are analogous to those for the Euler-Bernoulli beam model, as

$$\text{at } x=0 \rightarrow \begin{cases} EA \left(\frac{du}{dx} \right) = -F_1 & \text{or } u = \text{constant} \\ EI \left(\frac{d\Psi}{dx} \right) = -Q_1 & \text{or } \Psi = \text{constant} \\ GAKs \left(\Psi + \frac{dv}{dx} \right) = -S_1 & \text{or } v = \text{constant} \end{cases} \tag{8}$$

$$\text{at } x=L \rightarrow \begin{cases} EA \frac{du}{dx} = F_2 & \text{or } u = \text{constant} \\ EI \left(\frac{d\Psi}{dx} \right) = Q_2 & \text{or } \Psi = \text{constant} \\ GAKs \left(\Psi + \frac{dv}{dx} \right) = S_2 & \text{or } v = \text{constant} \end{cases}$$

Solution of these expressions (performed here in MAPLE v.6.0) provided the results of Figs. 4 and 5. In these plots, we required
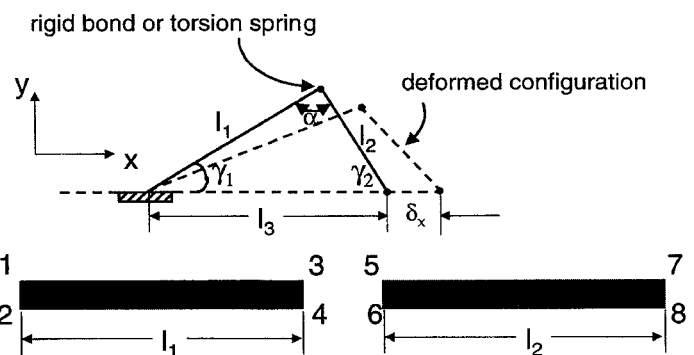
$$l_1 + l_2 = 1 \tag{9}$$

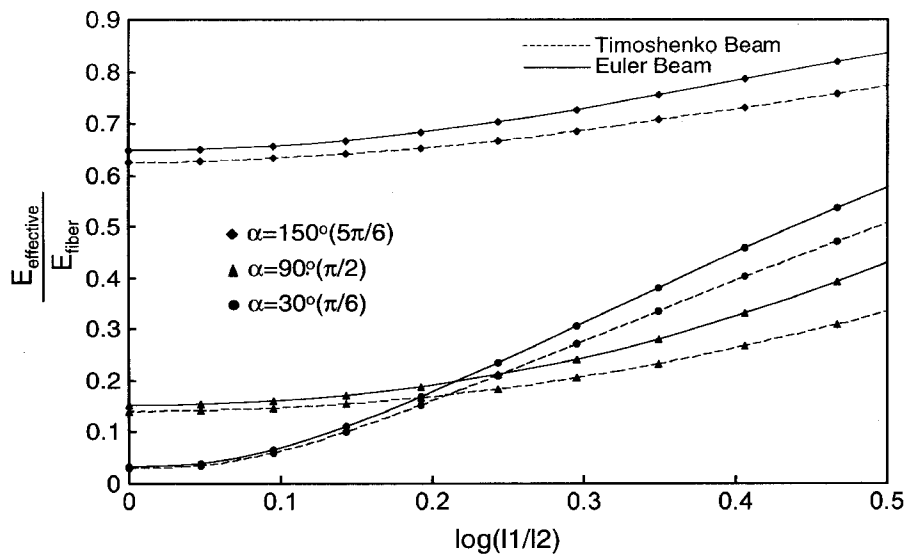Fig. 3 Two-beam network analyses notation

Fig. 4 Two-beam structural moduli, with notation of Fig. 3, for α=30, 90 and 150 deg, plotted for varying beam lengths as $\log(l_1/l_2)$. Nodes between segments are rigid. Euler-Bernoulli and Timoshenko beam results are compared in each case; two-beam assemblies are comprised of segments of diameter d=0.2.

and defined

$$E_{\text{effective}} = \left[\frac{\delta_x}{l_1 \cos \gamma_1 + l_2 \cos \gamma_2} \right] \sigma_x \qquad (10)$$

with maximum stress defined as the combined stress due to tension/compression and bending in the assembly, occuring at one of the nodal points shown in Fig. 3. Both plots are for a beam aspect ratio of $(l_1 + l_2)/d_{\text{segment}} = 5$ (i.e., $d_{\text{segments}} = 0.2$), for which the Euler-Bernoulli and Timoshenko beams would be expected to differ in prediction of loads/displacements. These simple examples illustrate that for rigidly connected beams, differences are only significant when one of the two segments is very short. Differences in effective moduli for the two beam types differ signifi-

cantly only when one segment is approximately one-half the length of the other, i.e. the shorter segment is of aspect ratio of approximately 1–2. Thus, for the range of applicability of beam theory, it probably is of marginal benefit even for rigidly connected beam assemblies, to better estimate their transverse shear stresses. In Part II, we describe the occurrence and loads in such short segment-beams, as they affect network properties.

2.3 Node Assumptions: Torsion Springs. In our earlier work, we described a technique for modeling network response using segments joined by torsion springs [18,19]. We repeat the main steps here for the Euler-Bernoulli beam, and also outline the procedure for the Timoshenko beam. For the Euler-Bernoulli case, we express the potential energy of the system as
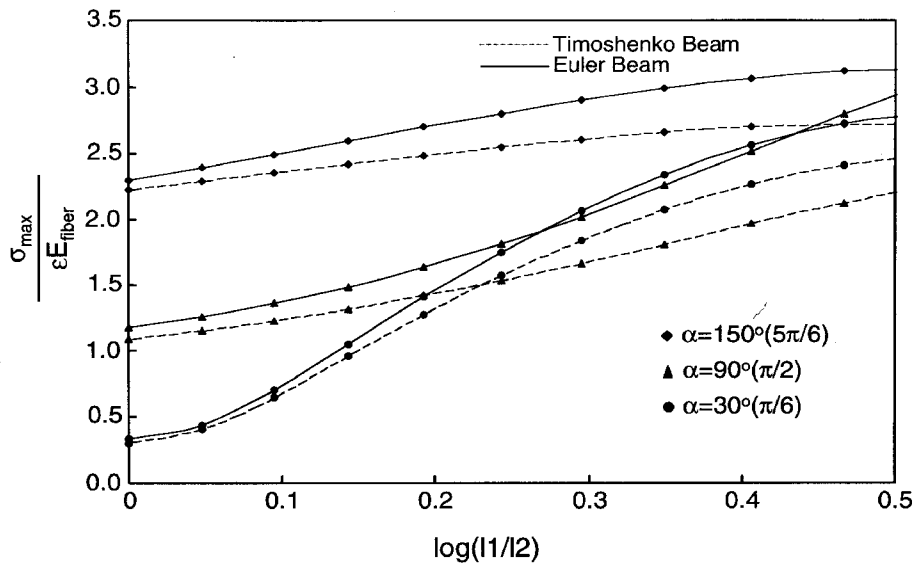

Fig. 5 Maximum loads in two-beam assemblies, with notation of Fig. 3, for α=30, 90 and 150 deg, plotted for varying beam lengths as $\log(l_1/l_2)$. Euler-Bernoulli and Timoshenko beam results are compared in each case; two-beam assemblies are comprised of segments of diameter d=0.2.

$$\pi = \frac{1}{2} \int_0^L \left[EA\left(\frac{du}{dx}\right)^2 + EI\left(\frac{d^2v}{dx^2}\right)^2 \right] dx + \frac{1}{2} K\left[\left(\frac{dv}{dx}\right)_{x=0} - \alpha_1 \right]^2$$

$$+ \frac{1}{2} K\left[\left(\frac{dv}{dx}\right)_{x=L} - \alpha_2 \right]^2 - F_1 u(0) - F_2 u(L) - S_1 v(0)$$

$$- S_2 v(L) - Q_1 \frac{dv(0)}{dx} - Q_2 \frac{dv(L)}{dx} \tag{11}$$

and the governing equations are obtained as

$$EA\frac{d^2u}{dx^2} = 0$$

$$EI\frac{d^4v}{dx^4} = 0 \tag{12}$$

Application of boundary conditions

$$\text{at } x=0 \rightarrow \begin{cases} EA\left(\frac{du}{dx}\right) = -F_1 & \text{or } u = \text{constant} \\[2mm] EI\left(\frac{d^2v}{dx^2}\right) - K\left[\left(\frac{dv}{dx}\right)_{x=0} - \alpha_1 \right] = -Q_1 & \text{or } \frac{dv}{dx} = \text{constant} \\[2mm] EI\left(\frac{d^3v}{dx^3}\right) = S_1 & \text{or } v = \text{constant} \end{cases} \tag{13}$$

$$\text{at } x=L \rightarrow \begin{cases} EA\frac{du}{dx} = F_2 & \text{or } u = \text{constant} \\[2mm] EI\left(\frac{d^2v}{dx^2}\right) + K\left[\left(\frac{dv}{dx}\right)_{x=L} - \alpha_2 \right] = Q_2 & \text{or } \frac{dv}{dx} = \text{constant} \\[2mm] EI\left(\frac{d^3v}{dx^3}\right) = -S_2 & \text{or } v = \text{constant} \end{cases}$$

allows solution for all internal loads and displacements.

For torsion-spring bonded Timoshenko beams, we have the potential energy

$$\pi = \left\{ \int_0^L \left[EA\left(\frac{du}{dx}\right)^2 \right] + \left[EI\left(\frac{d\Psi}{dx}\right)^2 \right] + GAKs\left(\Psi + \frac{dv}{dx} \right)^2 \right\} dx$$

$$+ \frac{1}{2} K_1\left(\frac{dv}{dx}_{x=0} + \Psi_{x=0} - \alpha_1 \right) + \frac{1}{2} K_2\left(\frac{dv}{dx} + \Psi - \alpha_2 \right)_{x=L}$$

$$- F_1 u(0) - F_2 u(L) - S_1 u(0) - S_2 u(L) - Q_1\Psi(0) - Q_2\Psi(L) \tag{14}$$

which, by the variational method, yields the governing equations

$$EA\frac{d^2u}{dx^2} = 0$$

$$EI\frac{d^2\Psi}{dx^2} - GAKs\left(\Psi + \frac{dv}{dx} \right) = 0 \tag{15}$$

$$GAKs\frac{d}{dx}\left(\Psi + \frac{dv}{dx} \right) = 0$$

Application of boundary conditions

$$\text{at } x=0 \rightarrow \begin{cases} EA\left(\frac{du}{dx}\right) = -F_1 & \text{or } u = \text{constant} \\[2mm] EI\left(\frac{d\Psi}{dx}\right) - K_1\left(\frac{dv}{dx} + \Psi - \alpha_1 \right) = Q_1 & \text{or } \Psi = \text{constant} \\[2mm] GAKs\left(\Psi + \frac{dv}{dx} \right) = -S_1 & \text{or } v = \text{constant} \end{cases}$$

$$\tag{16}$$

$$\text{at } x=L \rightarrow \begin{cases} EA\frac{du}{dx} = F_2 & \text{or } u = \text{constant} \\[2mm] EI\left(\frac{d\Psi}{dx}\right) + K_2\left(\frac{dv}{dx} + \Psi - \alpha_2 \right) = Q_2 & \text{or } \Psi = \text{constant} \\[2mm] GAKs\left(\Psi + \frac{dv}{dx} \right) = S_2 & \text{or } v = \text{constant} \end{cases}$$
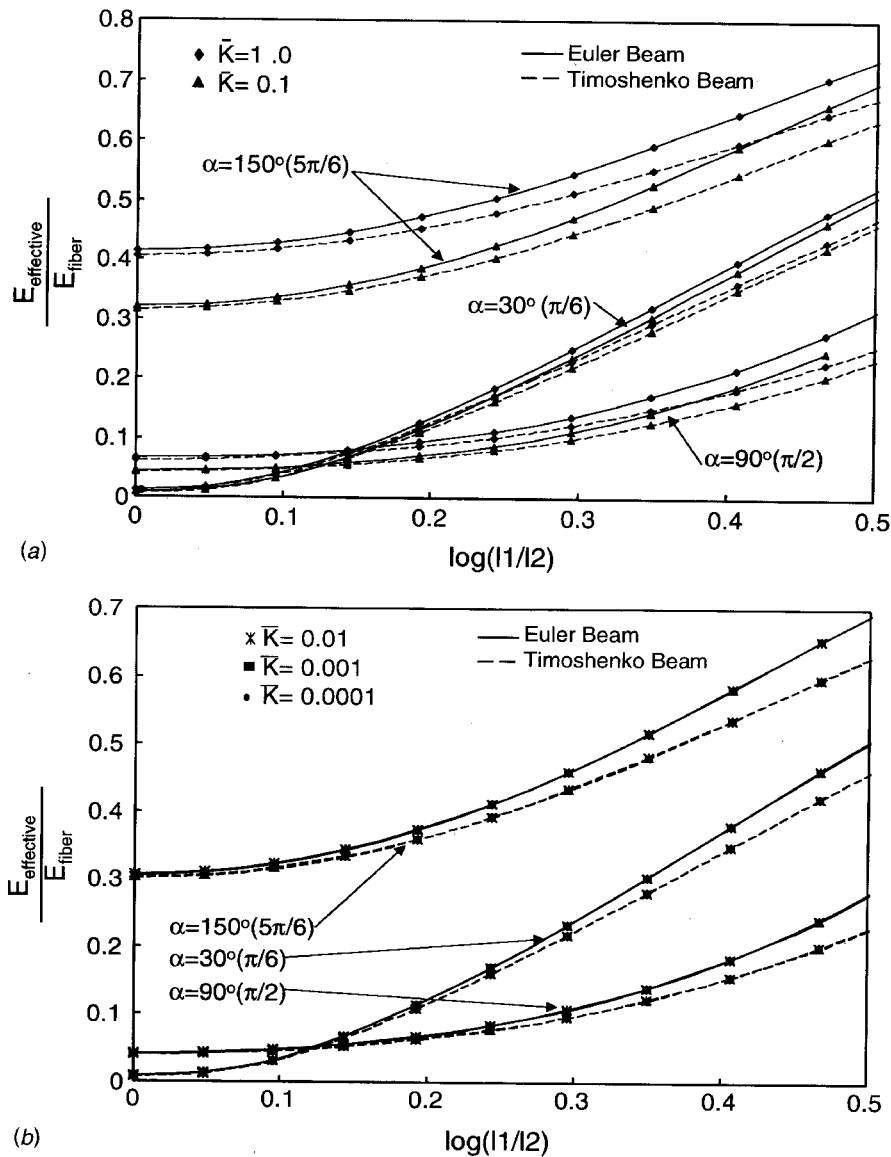
Fig. 6 Two-beam structural moduli, with notation of Fig. 3, for $\alpha=30$, $\alpha=90$ and $\alpha=150$ deg, plotted for varying beam lengths as $\log(l_1/l_2)$. Segments are joined by torsion springs, (a) for normalized spring constants 1.0 and 0.1, and (b) for normalized spring constants 0.01, 0.001, and 0.0001. Euler-Bernoulli and Timoshenko beam results are compared in each case; two-beam assemblies are comprised of segments of diameter $d=0.2$.

allows solution for all internal loads and displacements.

Solution of these expressions (performed here in MAPLEv.6.0 for the Euler-Bernoulli beam and in ABAQUS for the Timoshenko beam) provided the results of Figs. 6 and 7. In both plots, the torsion spring constant is normalized as

$$\bar{K} = \frac{Kl}{EI} \qquad (17)$$

where K is the torsion spring constant, l is the total beam length ($l = l_1 + l_2$), and E and I are the usual modulus and moment of inertia. Both plots are again for a beam aspect ratio of ($l_1 + l_2$)/$d_{\text{segment}} = 5$ (i.e., $d_{\text{segments}} = 0.2$). The compliance afforded by the torsion springs at the joints (which model imperfect bonds) reduces dramatically the importance of transverse shear in calculation of the stiffness and maximum stress in the assembly. As shown in Figs. 6 and 7 for effective modulus and maximum stress in such arrays, the dominant effect is the stiffness of the torsion spring constant, rather than the assumption of beam type. Clearly,

for more compliant torsion springs (i.e., normalized values of approximately 0.01 or less) the distinction between Euler-Bernoulli and Timoshenko beams is largely irrelevant.

By placement of the torsion springs at every segment, we neglect the higher stiffness afforded by fibers being continuous through intersections, e.g., we view a two-fiber intersection as a four-segment intersection, with attendantly greater overall compliance. The effect of this assumption is described presently in Part II of this work. However, the motivation for selection of the torsion spring to represent the intersecting region properties comes from an assumption about microstructure in the region around a fiber-fiber bond. These bonds are necessarily imperfect. Inclusion of a torsion spring allows some rotation of the fibers with respect to one another. Physically, this is not entirely realistic, though it is equivalent to a more realistic construct, described next.

2.4 Torsion Springs/Compliant Zone Equivalence. In the vicinity of a fiber-fiber intersection in substrate materials, we observe 1) incomplete intersection of the two fibers, i.e., fibers are
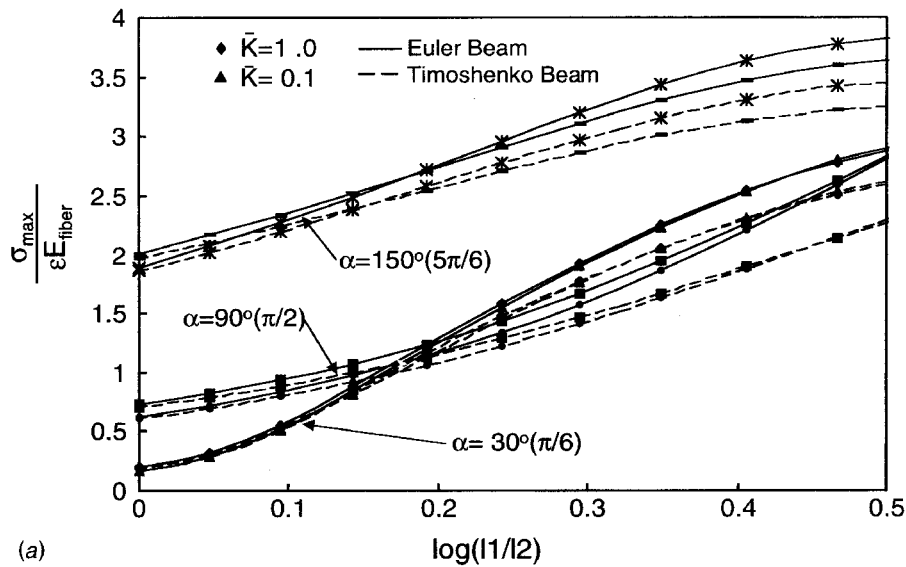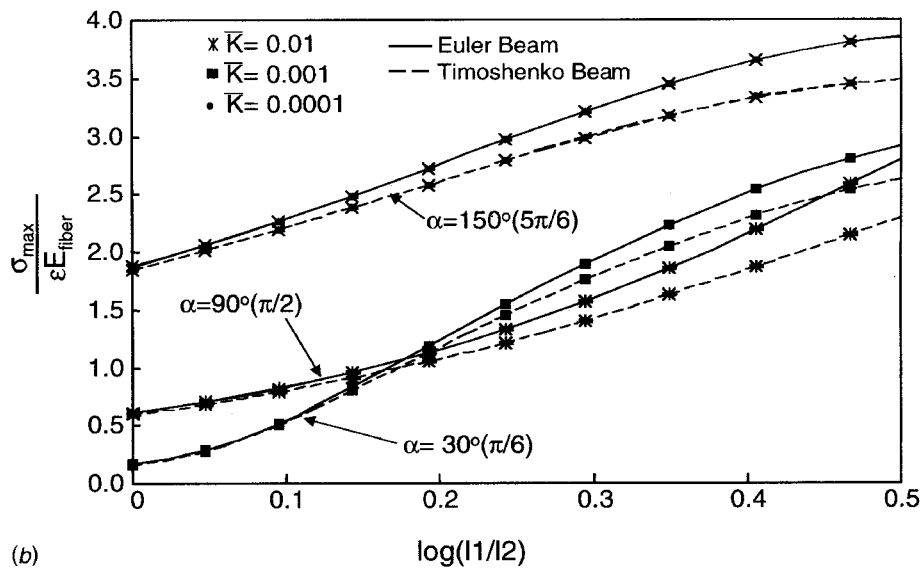
Fig. 7 Maximum loads in two-beam assemblies, with notation of Fig. 3, for α=30, α=90 and α=150 deg, plotted for varying beam lengths as $\log(l_1/l_2)$. Segments are joined by torsion springs, (a) for normalized spring constant 1.0 and 0.1, and (b) for normalized spring constant 0.01, 0.001, and 0.0001. Euler-Bernoulli and Timoshenko beam results are compared in each case; two-beam assemblies are comprised of segments of diameter d=0.2.

not fully "melted" into one another, and in the extreme, are bonded only at a point of tangency; and 2) a cluster of particles is often present at the intersection, so that the fibers themselves are not in contact, but they are joined by the particles (as shown schematically in Fig. 8(a)). The effects of the former observation are discussed in the Conclusions/Future Work section, as they may only be properly analyzed by a fully 3D analysis. The effect of the second phenomenon, however, can be determined by a 2D analysis as shown in Fig. 8(b), if the particle density of the bond is known or can be estimated from micrography or experiment. We can assume that this structure, rather than being comprised of two beams of common modulus, is instead an assembly of two multiphase beams, as in Fig. 8(a). We develop this model assuming that the regions close to the rigid bond are rather more compliant than the remainder of the beam, and denote the model as the "compliant zone model." However, the same arguments would apply for this simple linear system if for some reason the bond region were stiffened as compared to the beams.

Equivalence between the compliant zone model and the torsion spring model is shown in the following steps, with the torsion spring model shown in Fig. 9. The illustration of the two-beam models' equivalence can be easily extended to networks: the two beam cases are shown for simplicity. Two methods are shown for finding an equivalent compliant zone model (Fig. 8(b)) which has the same response to a given set of loads as a torsion spring model (Fig. 9) with a finite value of normalized spring constant K.

The beams in the compliant zone model (Fig. 8(b)) are of uniform cross-section. For the beam AB, the segment from A to D has elastic modulus E_1, while the remaining section DB of length b_2 has modulus E_2. The assembly is symmetric, so that for the beam BC, segment BE has modulus E_2, and section FC has modulus E_1. The beams are of equal, uniform cross-section. Since the model is symmetric, $\gamma_1 = \gamma_2$. The symbol γ is used in the equations to denote this angle.

The potential energy of the system in Fig. 8(b) can be written as

(a)

Fig. 9 Two-beam assembly of beams joined by a torsion spring at *B*
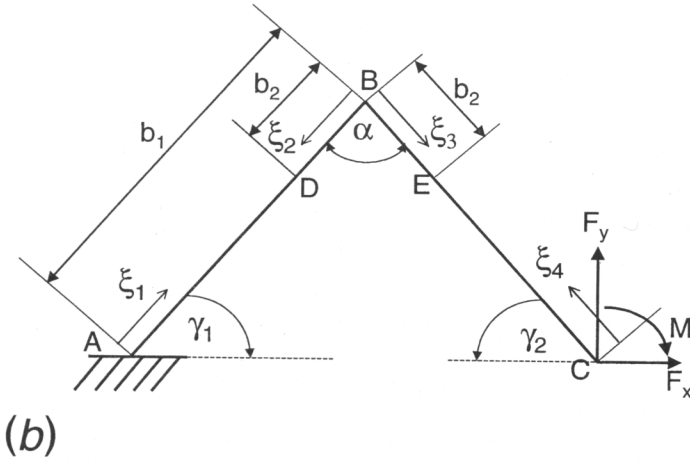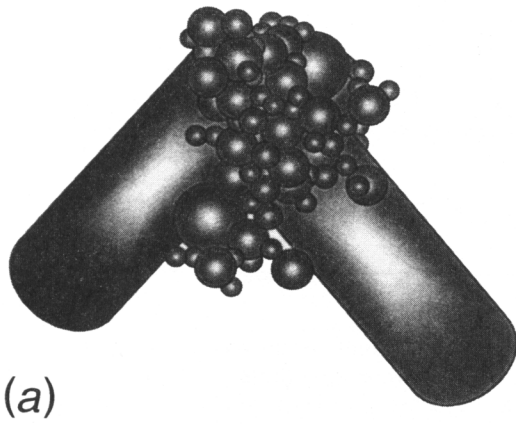

(b)

Fig. 8 A reduction of a physically realistic bond between fibers in a fiber/particle network to a 2D beam assembly (a), and notation for the two-beam assembly of rigidly joined beams, with each beam having a "compliant zone" of lengths b_2 (b)

with A, I, F, and M denoting the usual area, moment of inertia, force and moment.

The torsion spring model of Fig. 9 is comprised of two beams of length b_1 and Young's modulus, E with a torsion spring of spring constant K at the joint B. The cross-sections of the beams in this model are the same as that of the compliant zone model. Again γ is used in place of γ_1 and γ_2. The potential energy of the torsion spring assembly (Fig. 9) can be written as

$$U = \int_0^{b_1} \frac{F_{AB}^2}{2EA} + \frac{M_{AB}^2}{2EI} d\xi_1 + \int_0^{b_1} \frac{F_{BC}^2}{2EA} + \frac{M_{BC}^2}{2EI} d\xi_2 + \frac{M_{AB}(0)^2}{2K}$$

(19)

We apply a virtual displacement to the beam assembly, and calculate the loads (and thus effective structural modulus and maximum internal stress) as follows. For both systems, let X, Y, and Θ denote the horizontal, vertical and angular displacements respectively at point C. For either system, $X = \partial U / \partial F_x$, $Y = \partial U / \partial F_y$, $\Theta = \partial U / \partial M$. Subscripts 1 and 2 denote the model parameters, with 1 being the compliant zone model and 2 the torsion spring model.

We constrain our systems so that $Y = 0$ and $\Theta = 0$. For each system we can obtain expressions for the values of F_x, F_y, and M that which produce a displacement X in the horizontal direction, as

$$U = \int_0^{b_1 - b_2} \frac{F_{AD}^2}{2E_1 A} + \frac{M_{AD}^2}{2E_1 I} d\xi_1 + \int_0^{b_2} \frac{F_{DB}^2}{2E_2 A} + \frac{M_{DB}^2}{2E_2 I} d\xi_2$$

$$+ \int_0^{b_2} \frac{F_{BE}^2}{2E_2 A} + \frac{M_{BE}^2}{2E_2 I} d\xi_3 + \int_0^{b_1 - b_2} \frac{F_{EC}^2}{2E_1 A} + \frac{M_{EC}^2}{2E_1 I} d\xi_4$$
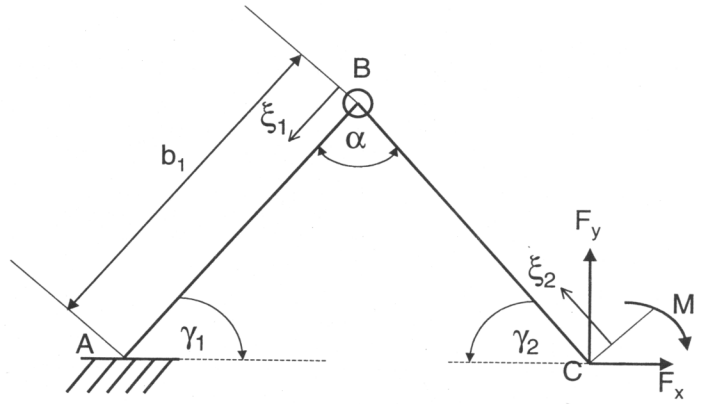
(18)

$$F_{x1} = \frac{6E_1 E_2 IA(E_1 b_2 + E_2(b_1 - b_2))X}{12I \cos(\gamma)^2 (E_2(b_1 - b_2) + b_2 E_1)^2 + A \sin(\gamma)^2 (E_2 - E_1)[E_2(b_1 - b_2)^4 - E_1 L_2^4] + AE_1 \sin(\gamma)^2 E_2 b_1^4}$$

(20)

$$F_{y1} = 0$$

(21)

$$M_1 = \frac{3E_1 E_2 IA \sin(\gamma)[E_2(b_1 - b_2)^2 + E_1 L_2(2b_1 - b_2)]X}{12I \cos(\gamma)^2 (E_2(b_1 - b_2) + b_2 E_1)^2 + A \sin(\gamma)^2 (E_2 - E_1)[E_2(b_1 - b_2)^4 - E_1 b_2^4] + AE_1 \sin(\gamma)^2 E_2 b_1^4}$$

(22)

$$F_{x2} = \frac{2EIA(2b_1 K + EI)X}{b_1[(b_1^3 AK \sin(\gamma)^2 + 12b_1 IK \cos(\gamma)^2) + 2b_1^2 EIA \sin(\gamma)^2 + 6EI^2 \cos(\gamma)^2]}$$

(23)

$$F_{y2} = 0$$

(24)

$$M_2 = \frac{3(EI + b_1 K)\sin(\gamma)^2 AEIX}{(b_1^3 AK \sin(\gamma)^2 + 12b_1 IK \cos(\gamma)^2) + 2b_1^2 EIA \sin(\gamma)^2 + 6EI^2 \cos(\gamma)^2}$$

(25)

For an equivalent system, we have

$$F_{x1}=F_{x2}, \qquad F_{y1}=F_{y2}, \qquad M_1=M_2 \tag{26}$$

Substituting Eq. (20)–Eq. (25) in Eq. (26) and solving simultaneously gives

$$E_1=\frac{2E(b_1-b_2)[\tan(\gamma)^2 A[E^2 I^2 b_1 b_2 - K^2 b_1^4 - 2EKb_1^2 I(b_1-b_2)] - 12IKL(EI+Kb_1)-3E^2 I^3]}{(b_2 IE + 2b_2 b_1 K - 2Kb_1^2)(6EI^2 + 2EA\tan(\gamma)^2 b_1^2 I + 12b_1 KI + AK\tan(\gamma)^2 b_1^3)} \tag{27}$$

$$E_2=\frac{-2Eb_2[\tan(\gamma)^2 A[E^2 I^2 b_1 b_2 - K^2 b_1^4 - 2EKb_1^2 I(b_1-b_2)] - 12IKb_1(EI+Kb_1)-3E^2 I^3]}{(b_2 IE + Ib_1 E + 2b_1 b_2 K)(6EI^2 + 2EA\tan(\gamma)^2 b_1^2 I + 12b_1 KI + AK\tan(\gamma)^2 b_1^3)} \tag{28}$$
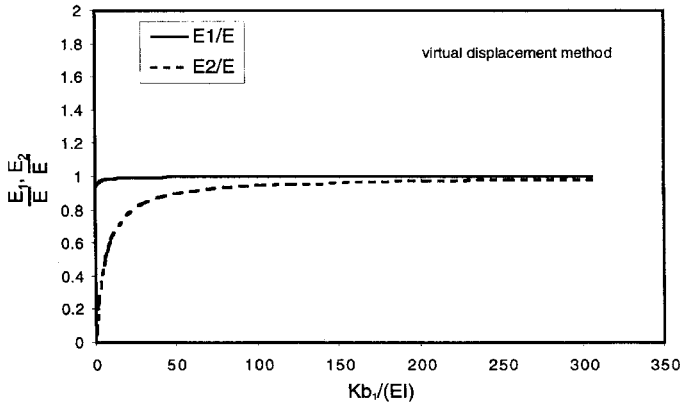

Fig. 10 Results for the virtual displacement method. Plots of moduli in compliant zones 1 and 2 versus normalized torsion spring constant, for the specific case of $b2=b1/10$. The solution for E_2 is singular as $K\to 0$ (load applied to segment 2).

For all positive values of E, I, A, K, and b_1, with $\alpha<180$ deg, F_{x2} and M_2 are positive. F_{x1} and M_1 must therefore be positive when Eq. (26) holds. Enforcing this condition results in the validity condition that

$$\frac{Kb_1}{EI}>\frac{b_2}{2(b_1-b_2)} \tag{29}$$

which is equivalent to requiring that both E_1 and E_2 are positive. Figure 10 is a graphical representation of these results for the specific case $b_2=b_1/10$. The modulus of the compliant zone in the beam on which the displacement is applied, E_2, is singular for this case as $K\to 0$.

3 Discussion

Porous networks comprised of elastic elements exhibit inelastic response at low strain, in addition to being susceptible to loss of percolation (and thus loss of meaningful conductivity) in the presence of even moderately small damage. The present authors have considered various models for both elements and connectivity in this paper, and in previous work. Euler-Bernoulli beams show satisfactory agreement with Timoshenko beams for rigidly-connected two-beam models examined here, with aspect ratios as low as 5. Both structural moduli and maximum stresses were examined, to allow investigation of element choice on stiffness and probable damage tolerance (Figs. 4 and 5).

Generally, it is recommended that deformation due to transverse shear be considered (i.e., Timoshenko beams be used) for beams of aspect ratios of around 5–10. Beam theory itself is only considered valid for beams of minimum aspect ratio ~ 10. That these models agree is not entirely a satisfactory reason for abandoning greater detail in models of the network elements; it only serves to illustrate that consideration of transverse shear deformation under these circumstances does not offer much insight. In Part II of this work, we underscore the recommendation that sim-

pler Euler-Bernoulli beam elements be used by examining the internal loads borne by these short elements in larger networks.

As expected, significant joint compliance only makes more detailed consideration of internal beam stresses less important, as much of the deformation in the assembly results from deformation at the torsion spring joint. Figures 6 and 7 illustrate this point for a wide range of (normalized) torsion spring constants, with even moderately high torsion spring constants, effectively eliminating the differences between the Euler-Bernoulli and Timoshenko two-beam assemblies.

Use of the torsion spring constant model provides a numerically simple adaptation to a rigidly-connected beam network to account for imperfect bonds. This is particularly important for fiber/particle networks, in which the particles may not themselves form a percolating, interconnected network, but nonetheless provide porous interconnects between fibers. A demonstration of how this linear model might be easily adapted to account for such connections, the compliant zone model, was presented here. These types of connections have been evident in many of the fiber/particle networks examined by the present authors, but such connections have been rather challenging to quantify in a satisfactorily statistically representative way. Undoubtedly, with improvements in computational speed and in image analysis, these will shortly be within reach. Adaptation of the linear model can be made to such multiphase networks as needed.

4 Conclusions/Future Work

We conclude that the simple beam approximation has a good basis when degenerate networks (two-beam) are considered. We illustrate the use of a linear torsion spring between beams as an approach to assigning a linear deformability to the intersection, and show its correspondence to one more physically realistic circumstance. Results here are tested in Part II of this work for large networks, and the effects of these various simple assumptions on material behavior is assessed. These illustrations show however, that more detailed assumptions in the beam theory framework are not merited.

In analysis of broad classes of particle/fiber networks, it is likely that consideration of 3D effects would be required, both in morphology (in terms of how non-percolated impenetrating phases might effect connectivity in a percolated phase, as in the particle/fiber networks motivating the present investigation). It also seems likely that small scale 3D analyses might yield significant insight such that a satisfactory 2D simulation approach might be designed. For a 2D or a 3D analysis, intersection of two fibers even only at a single point of tangency results in an identical effective, or structural modulus, for the assembly due to equilibrium considerations. In the 3D analysis of such an "imperfect" bond, we find, of course, that the maximum stress in the assembly is considerably higher in the case of less impenetration of fibers at a bond, due to the stress riser of the saddle-shaped intersection. The stress singularity arising at such interconnects, and methods for their analysis, are reserved for future work.

Acknowledgments

Nomenclature

A = cross-sectional area

A_s = shear area

b_1 = total length of each beam in compliant zone model (Fig. 8(b))

b_2 = length of "compliant zone" (Fig. 8(b))

$d_{segment}$ = diameter of a segment in a beam network

E = Young's modulus

E_1, E_2 = Young's moduli of segments of compliant zone model (Fig. 8(b))

$E_{effective}$ = effective Young's modulus of a beam assembly

F_1, F_2 = axial force (subscript denotes end at which it is applied)

F_{AB}, F_{BC} = axial forces in members AB and BC of torsion spring model (Fig. 9)

F_{AD}, F_{DB} = axial forces in members AD and DB of compliant zone model (Fig. 8(b))

F_{BE}, F_{EC} = axial forces in members BE and EC of compliant zone model (Fig. 8(b))

F_{x1}, F_{x2} = applied force at point C in x-direction. Subscript 1 denotes compliant zone model and 2, the torsion spring model (Figs. 8(b) and 9)

F_{y1}, F_{y2} = applied force at point C in y-direction. Subscript 1 denotes compliant zone model and 2, the torsion spring model (Figs. 8(b) and 9)

G = shear modulus

I = second moment of area

K = torsion spring constant

K_1, K_2 = torsion spring constant. Subscript denotes end at which spring is located

K_s = shear correction factor

L = beam length

l_c = length of a simulation cell size

l_1, l_2 = beam lengths (Fig. 3)

M_1, M_2 = applied moment at point C. Subscript 1 denotes compliant zone model and 2, the torsion spring model (Figs. 8(b) and 9)

M_{AB}, M_{BC} = moment in members AB and BC of torsion spring model (Fig. 9)

M_{AD}, M_{DB} = moment in members AD and DB of compliant zone model (Fig. 8(b))

M_{BE}, M_{EC} = moment in members BE and EC of compliant zone model (Fig. 8(b))

Q_1, Q_2 = bending moment (subscript denotes end at which it is applied)

S_1, S_2 = shear force (subscript denotes end at which it is applied)

u = x-direction displacement

v = y-direction displacement

X_1, X_2 = x-direction displacement of point C. Subscript 1 denotes compliant zone model and 2, the torsion spring model (Figs. 8(b) and 9)

U = strain energy

V = shear force

Y_1, Y_2 = y-direction displacement of point C. Subscript 1 denotes compliant zone model and 2, the torsion spring model (Figs. 8(b) and 9)

α_1, α_2 = internal rotation between two beams (subscripts denote end)

π = potential energy

Ψ = rotation function about the y-axis

Θ = angular displacement of point C. Subscript 1 denotes compliant zone model and 2, the torsion spring model (Figs. 8(b) and 9)

ξ_1, ξ_2, ξ_3, ξ_4 = local coordinates along beam segments of compliant zone and torsion spring models (Figs. 8(b) and 9)

α = angle between beams in two-beam assembly

γ_1, γ_2 = angles between beams of two-beam assembly and x-axis

τ_a = actual shear stress

References

[1] Sastry, A. M., Choi, S. B., and Cheng, X., 1998, "Damage in Composite NiMH Positive Electrodes," ASME J. Eng. Mater. Technol., **120**, pp. 280–283.

[2] Wang, C. W., and Sastry, A. M., 2000 "Structure, Mechanics and Failure of Stochastic Fibrous Networks: Part II-Network Simulations and Application," ASME J. Eng. Mater. Technol., **122**.

[3] Sastry, A. M., Cheng, X., and Wang, C. W., 1998, "Mechanics of Stochastic Fibrous Networks," J. Thermoplast. Compos. Mater., **30**, pp. 288–296.

[4] Hashin, Z., 1962, "The elastic moduli of heterogeneous material," ASME J. Appl. Mech., **29**, pp. 143–150.

[5] Christensen, R. M., and Lo, K. H., 1979, "Solutions for effective shear properties in three phase sphere and cylinder models," J. Mech. Phys. Solids, **27**, pp. 315–330.

[6] Meridith, R. E., and Tobias, C. W., 1962, "II Conduction in Heterogeneous Systems," Advances in Electrochemistry and Electrochemical Engineering, Interscience, New York, pp. 15–47.

[7] Cox, H. L., 1952, "The Elasticity and Strength of Paper and Other Fibrous materials," Br. J. Appl. Phys., **3**, pp. 72–79.

[8] Backer, S., and Petterson, D. R., 1960, "Some Principles of Nonwoven Fabrics," Text. Res. J., **30**, pp. 704–711.

[9] Niskanen, K., 1993, "Strength and Fracture of Paper," Products of Papermaking: Transactions of the Tenth Fundamental Research Symposium, PIRA International, United Kingdom, Vol. 2, pp. 641–725.

[10] Hearle, J. W. S., and Newton, A., 1968, "Part XV: The Application of the Fiber Network Theory," Text. Res. J., **1**, pp. 343–351.

[11] Hearle, J. W. S., 1980, "The Mechanics of Dense Fibre Assemblies," The Mechanics of Flexible Fibre Assemblies, Hearle, J. W. S, Thwaites, J. J., and Amirbayat, J., eds., Sijthoff and Noordhoff, New York, pp. 51–86.

[12] Ostoja-Starzewski, M., Sheng, P. Y., and Jasiuk, I., 1994. "Influence of Random Geometry on Effective Properties and Damage Formation in Composite Materials," ASME J. Eng. Mater. Technol., **116**, pp. 384–391.

[13] Alzebdah, K., and Ostoja-Starzewski, M., 1996, "Micromechanically based stochastic finite elements: length scales and anisotropy," Probab. Eng. Mech., **11**, pp. 205–214.

[14] Lu, W., Carlsson, L. A., and Andersson, Y., 1995, "Micro-Model of Paper, Part 1: Bounds on Elastic Properties," Tappi J., **78**, pp. 155–164.

[15] Lu, W., and Carlsson, L. A., 1996, "Micro-Model of paper, Part 2: statistical analysis of the paper structure," Tappi J., **79**, pp. 203–210.

[16] Lu, W., Carlsson, L. A., and de Ruvo, A., 1996, "Micro-Model of paper, Part 3: Mosaic model," Tappi J., **79**, pp. 197–205.

[17] Curtin, W. A., 1990, "Lattice Trapping of Cracks," J. Mater. Res., **5**, pp. 1549–1560.

[18] Cheng, X., and Sastry, A. M., 1999, "On Transport in Stochastic, Heterogeneous Fibrous Domains," Mech. Mater., **31**, pp. 765–786.

[19] Wang, C. W., Cheng, X., Sastry, A. M., and Choi, S. B., 1999, "Investigation of Failure Processes in Porous Battery Substrates: Part 1—Experimental Findings," ASME J. Eng. Mater. Technol., **121**, pp. 503–513.

[20] Cheng, X., Sastry, A. M., and Layton, B. E., 2000, "Transport in Stochastic Fibrous Networks," ASME J. Eng. Mater. Technol., accepted.

[21] Cheng, X., Wang, C. W., Sastry, A. M., and Choi, S. B., 1999, "Investigation of Failure Processes in Porous Battery Substrates: Part II—Simulation Results and Comparisons," ASME J. Eng. Mater. Technol., **121**, pp. 514–523.

[22] Kirkpatrick, S., 1973, "Percolation and conduction," Rev. Mod. Phys., **45**, No. 4, pp. 574–588.

[23] Reddy, J. N., 1993, An Introduction of the Finite Element Method, McGraw-Hill, Vol. 2, New York, pp. 177–191.

[24] Bathe, K. J., 1996, Finite Element Procedures, Prentice-Hall, Englewood Cliffs, NJ, pp. 399–400.